Journal of Power Sources 222 (2013) 359–366

Contents lists available at SciVerse ScienceDirect

Journal of Power Sources

journal homepage: www.elsevier.com/locate/jpowsour

Elastic configurations of self-supported oxide membranes for fuel cells

K. Kerman [a,*,1], T. Tallinen [a,c,1], S. Ramanathan [a], L. Mahadevan [a,b]

[a] School of Engineering and Applied Sciences, Harvard University, Cambridge, MA, USA
[b] Department of Physics, Harvard University, Cambridge, MA, USA
[c] Department of Physics, University of Jyväskylä, P.O. Box 35, FI-40014 Jyväskylä, Finland

HIGHLIGHTS

- Address the origin for far-from threshold buckling patterns in self-supported oxide membranes.
- Provide an outline of shape evolution based on reduced stress.
- Corroborate results of elastic model with experimental fabrication of self-supported thin film YSZ membrane.
- Utilize self-supported membrane to show a proof-of-concept thin film SOFC operating directly with natural gas.
- Obtain near-ideal open circuit potential, indicating pristine nature of membrane.

ARTICLE INFO

Article history:
Received 23 June 2012
Received in revised form
30 August 2012
Accepted 31 August 2012
Available online 10 September 2012

Keywords:
Buckling
Oxide membrane
Self-supported membrane
Thin film
SOFC
Natural gas

ABSTRACT

Ultra-thin oxide films are of interest in energy conversion technologies such as low temperature solid oxide fuel cells and permeation membranes. Understanding their thermo-mechanical stability is an important problem. Edge clamped, self-supported thin film membranes show hierarchical wrinkles; with the largest wavelengths in the center, while smaller ones arise near the clamped boundary; correspondingly the largest strains, with tensile stress comparable to the residual stress, are in the vicinity of the clamped boundary. Our results can be understood by simple scaling arguments and are valid for membranes in the post-buckling regime far from threshold. We confirm the validity of our analysis by quantitative experimental comparison to self-supported, square micro-machined yttria-stabilized zirconia membranes of edge length 160 μm fabricated by lithography. The modeling and experiments combined provide a foundation for designing failure resistant self-supported membranes of interest to energy conversion. We show this by utilizing such membranes to fabricate thin film solid oxide fuel cells and demonstrate power generation utilizing natural gas as fuel at ~400 °C.

1. Introduction

Ultra-thin membranes are of broad interest in electrochemical energy devices that are generally comprised of an electrolyte that selectively conducts ionic species with catalytically active electrodes on either side. Transport of O^{2-} ions through typical electrolytes for solid oxide fuel cells (SOFCs) is a thermally activated process and often requires temperatures in the 800–1000 °C range to obtain substantial current [1]. Such high temperature operation is detrimental for start-up time, sealing, material degradation, and cost. The oxygen flux per unit area can be expressed by $j = \sigma_i \mathrm{d}\phi/\mathrm{d}x$ where σ_i and $\mathrm{d}\phi/\mathrm{d}x$ represent the ionic conductivity and linear voltage gradient across the electrolyte, respectively [2]. In the limit $\mathrm{d}\phi/\mathrm{d}x = \phi/h$, where ϕ is the cell voltage and h is the electrolyte thickness, it can be deduced that the resistance takes a form similar to Ohm's law and that it is directly proportional to h. Thus, reducing the electrolyte thickness allows a significant reduction in the operating temperature by decreasing the Ohmic resistance across the electrolyte associated with ionic flux. In order to explore the ultimate limits of this reduction, ultra-thin oxide membranes must be fabricated. From an electrochemical perspective, the thin membrane must not have an electronically conductive path through the thickness and it must be defect free to avoid electronic shortage or reactant mixing, respectively; either of which can be deleterious to high performance application and safety. Furthermore, in reducing the thickness to the nanometer scale, mechanical stress, stability, and survivability must also be rigorously investigated.

* Corresponding author.
E-mail address: kkerman@fas.harvard.edu (K. Kerman).
[1] Equal contribution.

0378-7753/$ – see front matter © 2012 Elsevier B.V. All rights reserved.
http://dx.doi.org/10.1016/j.jpowsour.2012.08.092

Preliminary geometrical constraints of thin self-supported membranes for such applications deemed buckling as mechanical failure [3]. By considering non-linear stress analysis it was later suggested that a larger design space in the post-buckling regime exists, however, only bounds for stable near-threshold, i.e. first and second buckling modes, were considered [4]. There has been much research on thin film SOFCs utilizing oxide membranes, mostly without consideration for the higher order buckling modes [5–9]. A recent investigation addressed the commonality of buckling in oxide membranes used for thin film SOFCs [10]. However, quantitative numerical modeling was limited to compressions in the 0.5–300 MPa range. The residual compressive stress of yttria-stabilized zirconia thin films sputtered at room temperature has been reported to be greater than 500 MPa for thicknesses below 100 nm [11]. In this contribution, we present a combination of numerical and experimental results that addresses the stable configuration of such self-supported oxide membranes and includes a spatial distribution of calculated principle stresses which are useful for failure analysis. We further present scaling behavior at relevant compressions that is broadly applicable to self-supported membranes across a wide size range. Lastly, we integrate the self-supported membranes into thin film SOFCs that operate with natural gas fuel and show near ideal thermodynamic voltage, confirming the stability and pristine nature of the elastically buckled membranes.

2. Elastic buckling and modeling

Buckling of a compressed square plate at small strains can be analyzed by the energy method of classical stability analysis. With clamped boundary conditions, the critical biaxial buckling stress is $\sigma_{cr} \approx (4.39/(1-\upsilon^2))E(L/h)^{-2}$ and out-of-plane amplitude after buckling is given by $w_{max} \approx 0.52\sqrt{(\sigma_0/E)}L$, where L, h, E and ν represent edge length, thickness, modulus of elasticity and Poisson's ratio, respectively [12]. However, the classical analysis describes only the first buckling mode for the magnitude of the residual stress, $\sigma_0 \geq \sigma_{cr}$, just above the critical buckling threshold. In thin film membranes σ_0 is typically much higher than σ_{cr} and post-buckling far from the threshold must be considered. For $\sigma_0 \gg \sigma_{cr}$ the compressive stress of the membrane relaxes by buckling in the vicinity of the clamped boundary [12,13]. The basic principle of the stress relaxing boundary layer is best understood by a simple scaling analysis. In-plane compression relaxes over a width δ by out-of-plane buckling. The buckling has a wavelength λ; amplitude $A \sim \lambda\sqrt{\sigma_0/E}$; curvatures $C_{\parallel} \sim A/\lambda^2 \sim (\sqrt{\sigma_0/E})/\lambda$ and $C_{\perp} \sim A/\delta^2 \sim (\lambda\sqrt{\sigma_0/E})/\delta^2$ in directions parallel and perpendicular to the boundary, respectively; in plane energy per unit length of the boundary $S \sim (h\delta\sigma_0^2)/E$; and bending energy $B \sim Eh^3\delta(C_{\parallel}^2 + C_{\perp}^2) \sim h^3\delta((\sigma_0/\delta^2) + (\lambda^2\sigma_0/\delta^4))$. Minimizing the sum of in-plane and bending energy, $U = S + B$, by requiring $\partial U/\partial\delta = \partial U/\partial\lambda = 0$ yields $\lambda \sim \delta \sim h/(\sqrt{\sigma_0/E})$. The wavelength of buckling is coarsened by a series of periodic steps moving from the boundary layer toward the interior of the membrane. Similar coarsening occurs for general cases of compressed sheets [14–17].

To study buckling and mechanical patterns of the membranes quantitatively, a numerical model of a compressed elastic membrane having clamped boundaries was used. The model has previously been used to study compression of thin-walled structures under general loading conditions [16]. It consists of a square lattice with spacing a. Each square is divided into two triangles along the diagonal such that the diagonal edges of length $\sqrt{2}a$, form a grid of squares rotated by $\pi/4$ with respect to the original lattice. The in-plane strain is determined from the relative positions of the nodes of such triangles. A constitutive relation of stress and strain for an isotropic elastic material is applied to determine the in-plane stress and accordingly, the corresponding forces on the nodes. Large displacements and rotations are taken into account in the formulation, so as to correctly describe geometrically non-linear deformations of the membrane. The resistance to bending deformations for the membrane is introduced via an energetic cost $J(1 - \hat{n}_i \cdot \hat{n}_j)$ for each pair of adjacent triangles with normals $\hat{n}_i$ and $\hat{n}_j$, with J representing the bending stiffness. This is consistent with a continuum theory for the deformations of a naturally flat surface on to one with curvature C, which requires an energy density $\frac{1}{2}\kappa C^2$, where the constant J is $J = \kappa$ for the pairs of triangles that share an edge of length a, and $J = \sqrt{2}\kappa$ for the diagonal pairs. Here $\kappa = Eh^3/(12(1-\nu^2))$, which is the bending modulus of the membrane. An explicit method is used to solve the damped Newtonian dynamics of the nodes, each of them having mass $m = a^2h$. Compression of the membrane is implemented by imposing a biaxial in-plane strain $(\sigma_0(1-\nu))/E$ in the flat initial configuration.

Buckling amplitude of the membranes can be large, but gradients of out-of-plane displacement are still small, which implies that deformation patterns are functions of the scaled stress $\tilde{\sigma}_0 = (\sigma_0/E)(L/h)^2$ only, assuming a fixed Poisson ratio, $\nu = 0.3$. This result, following from re-scaling of the von Karman energy function [13,18], greatly simplifies the numerical task. L/h can be fixed and only σ_0 needs to be varied to cover the whole experimentally relevant parameter range. A lattice of 320 × 320 sites with spacing $a = 3.13h$, corresponding to $L/h = 1000$, was used. The role of the residual stress was studied by gradually increasing σ_0 from zero to $\sigma_0 = 0.047E$, which corresponds to $\tilde{\sigma}_0$ increasing from zero to $\tilde{\sigma}_0 = 4.7 \times 10^4$.

3. Fabrication of self-supported membrane and fuel cells

To directly compare simulation results to experiment, thin films of 8 mol% yttria-stabilized zirconia (YSZ), a prototypical electrolyte used for high temperature electrochemical energy devices such as SOFCs, were grown at 550 °C by radio-frequency (RF) sputtering at a deposition rate of 2.2 nm min^{-1} on Si_3N_4 coated Si substrates. Substrates were lithographically patterned and subsequently etched to reveal small windows of side length, $L = 160$ μm. The processing scheme is as follows: photolithography to pattern Si_3N_4, dry etching to remove the patterned area and expose Si, and finally wet etching in KOH to selectively remove Si. Further details on the fabrication method of these membranes and devices incorporating them can be found elsewhere [9]. After film growth, the YSZ film was released in such windows by removing the final Si_3N_4 layer by reactive ion etching to create a self-supported, clamped membrane structure with defined edge length. The phase purity and thickness of the films were verified by X-ray diffraction and X-ray reflectivity, respectively. Optical and confocal microscopy was used to observe the buckling patterns and quantify the out-of-plane displacements, respectively. Scanning electron microscopy was used to investigate the microstructural characteristics of the films. As-deposited film stress was estimated by a wafer curvature technique, which relates a difference in curvature of the wafer before and after film deposition to residual stress, σ_0, by Stoney's formula, $\sigma_0 = (E_s/1-\nu_s)(\Delta K/6)(h_s^2/h_f)$; [19]; where $E_s/(1-\nu_s)$, ΔK, h_s, h_f, are the substrate biaxial modulus, change in curvature, substrate thickness, and film thickness, respectively.

Integration of the self-supported thin film electrolytes into thin film SOFCs (TF-SOFCs) was done by depositing an active electrocatalytic metal on either side of the membrane. Nano-porous Pt was deposited symmetrically on both sides of the membrane by direct current sputtering without substrate heating at an Ar pressure of 75 mTorr. Fuel cell testing was then carried out in a custom built two-chamber test station that flowed pure natural gas at a rate of

30 cm^3 min^{-1} on one side of the membrane while the other was exposed to standing laboratory air. The electrolyte membrane is physically sealed to the substrate if there are no voids or cracks in the film. The substrate is then fastened using a gold ring and circular clamp to ensure no fuel leakage during measurement. Open circuit voltage (OCV) and *I–V* data was generated in galvanostatic mode and using a linear voltage sweep, respectively. Further details can be found in our previous work on this type of experimental platform [9].

4. Results and discussion

The initial structural X-ray characterization of the polycrystalline films studied in this investigation is shown in Fig. 1(a). It can be seen that the YSZ films are phase pure and (111) textured. The out of plane lattice parameters are plotted in Fig. 1(b)–(d) as a function of thickness. From these figures it is clear that there is thickness dependence of lattice constant likely due to residual stresses in the film. Since the films are not coherently strained to the substrate, the origin of these residual stresses can be related to atomic peening during initial stages of film growth [20]. From the tabulated value for YSZ, the unstrained lattice parameter is also plotted as a dashed line [21]. Using a linear fit to each of the three families, the expected unstrained thickness can be estimated. An average thickness value of ~240 nm should be nearly strain free. The direct experimental measurement and scaling of the residual film strain are discussed in Section 4.1. For reference and clarity, a graphical description of the processing procedure and simulated depiction of the self-supported membranes studied are shown in Fig. 2(a) and (b), respectively.

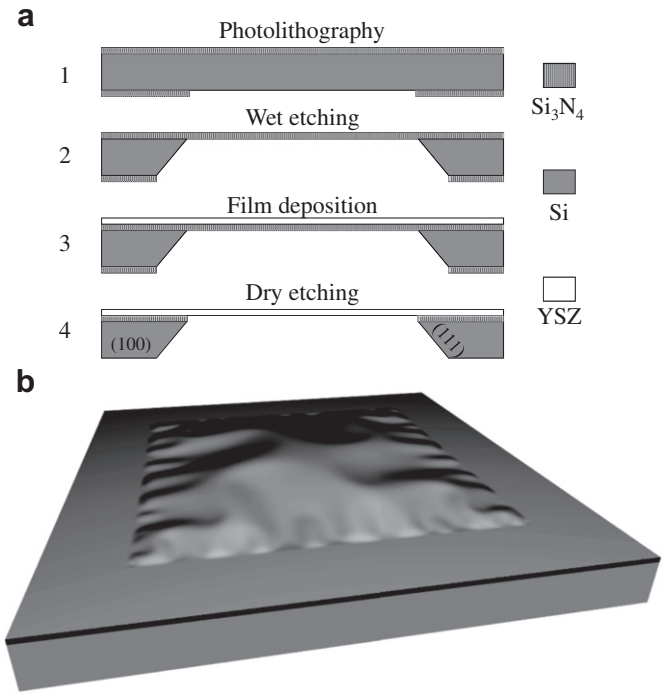

Fig. 2. (a) Schematic of process flow used to create the self-supported thin film structure studied and used in thin film SOFCs, and (b) 3-D computational simulation of such a membrane.

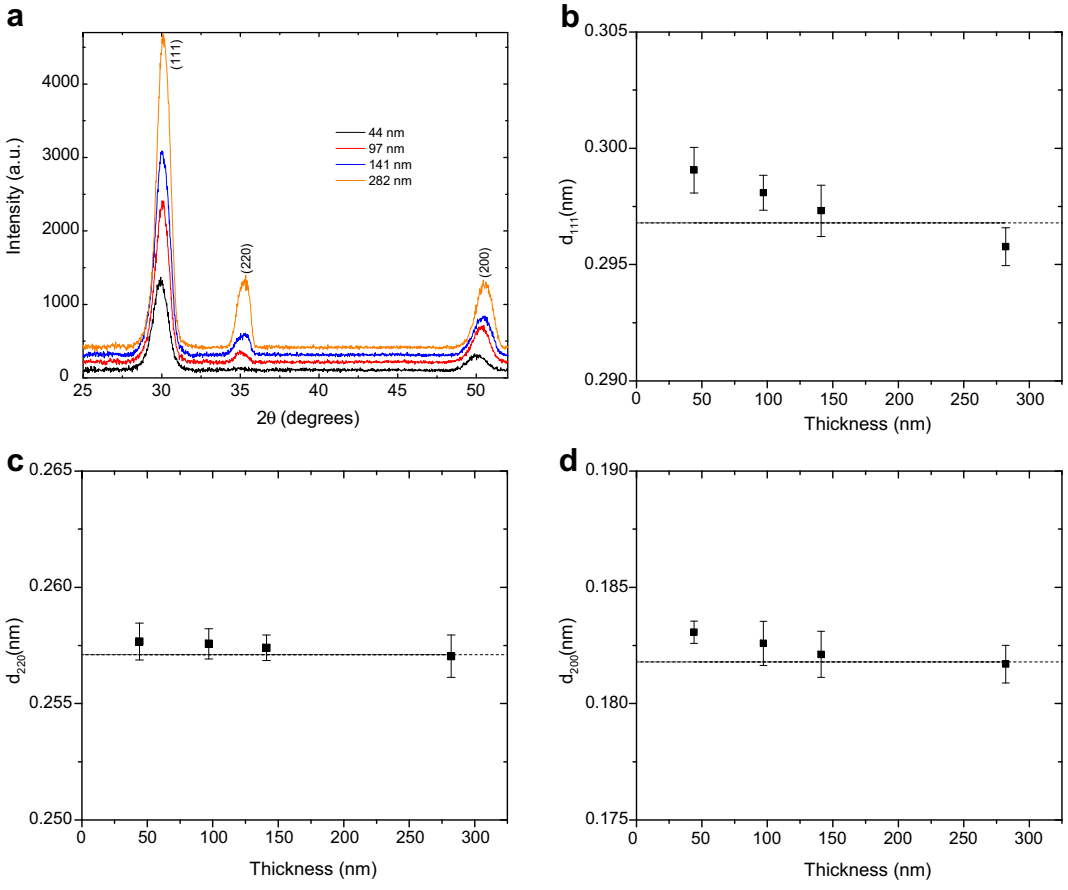

Fig. 1. (a) X-ray diffraction patterns of select YSZ films showing the single phase crystallinity, indexed to ICDD-030-01468. The out-of-plane lattice parameter of (b) (111), (c) (220), and (d) (200) as a function of film thickness with dashed lines depicting the ICDD lattice parameter value. Error bars correspond to ±3 standard deviations.

The remainder of this study relates to the experimental and modeling results for self-supported oxide membranes and the demonstration of TF-SOFCs using a 100 nm thick self-supported YSZ membrane.

4.1. Membrane elastic configurations

At a fixed clamped side length, σ_0 can be engineered by adjusting deposition parameters, post-deposition annealing conditions, or film thickness [11]. Fig. 3(a)–(c) shows optical and confocal micrographs of a series of self-supported YSZ membranes with varying σ_0. Fig. 3(d) shows the total residual film stress as a function of thickness for as-deposited YSZ films. All films exhibit compressive residual stress with monotonically decreasing magnitude as the thickness increases. Based on the approximate estimation of strain state from the X-ray results in Fig. 1, it was expected that the films thicker than ~240 nm would be nearly strain free. As seen in Fig. 3(d), this is not exactly the case. One possibility for this slight discrepancy includes the fact that only three orientations were used to make this assertion, but since the film is polycrystalline all orientations play a role in strain behavior of the film. Additionally, it is known that there can be error in lattice parameter estimations at low diffraction angles since a small measurement error can result in a large lattice parameter miscalculation. The slope of the linear fit to each family appears to reduce as the diffraction peak position increases in angle, therefore the strain free thickness calculation from this method may be an underestimate. The last consideration is that the method of wafer curvature becomes inappropriate at very small curvatures, or low film stress, therefore the error associated with smaller stresses becomes a substantial fraction of the actual value [22]. Nevertheless, a significant variation in macroscopic buckling patterns is seen as σ_0 is varied. The thinnest film exhibits the largest compressive σ_0 and therefore can be instrumental in determining a ground-state buckling configuration. Fig. 4(a) depicts the steady state buckling pattern obtained by simulation. The simulation and experimental results are similar, confirming that a simple elastic theory suffices to understand how the patterns are formed. The simulated buckled configuration at small $\tilde{\sigma}_0$, immediately after first buckling, is symmetric with respect to diagonal reflections. However, the symmetric configuration persists only up to $\tilde{\sigma}_0 \approx 4 \times 10^2$, beyond which the pattern changes to a swastika-like appearance shown in Figs. 3(c) and 4(a). Further increase of $\tilde{\sigma}_0$ in simulations does not change the pattern in the interior of the membrane; though the amplitude increases and wavelength at the boundary refines. Indeed, this appears to corroborate the classic work on mechanical response of micro-machined Si_3N_4 square membranes done by Ziebart et al. [23] Their work shows the transition to the swastika-like pattern at pre-strain that corresponds to $\tilde{\sigma}_0 \approx 3 \times 10^2$ and the pattern persists with sharpened refinements as the strain is increased. The out-of-plane amplitude in Fig. 4(c) is approximated well by the above expression for w_{max} even when $\sigma_0 \gg \sigma_{cr}$.

Not all membranes display the kind of pattern shown in Fig. 3(c) after the Si_3N_4 support has been removed. Fig. 3(b) shows that in

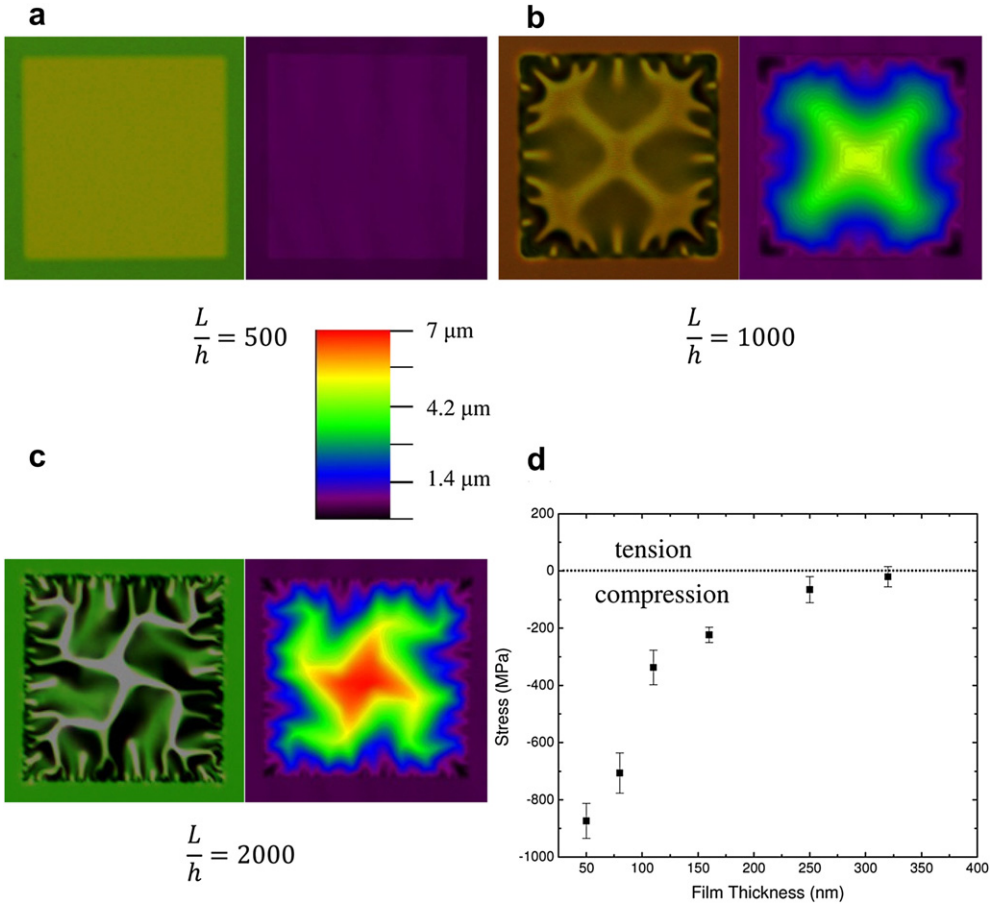

Fig. 3. (a–c) Experimental optical and confocal micrographs of self-supported thin film YSZ membranes, 160 μm in edge length, with varying L/h indicated. Beyond a critical thickness, experimental observation indicates that membranes tend toward a pattern similar to that in (c). The total stress measured in as-deposited YSZ films measured by wafer curvature as a function of thickness is shown in (d). Error bars correspond to ±3 standard deviations for average values plotted.

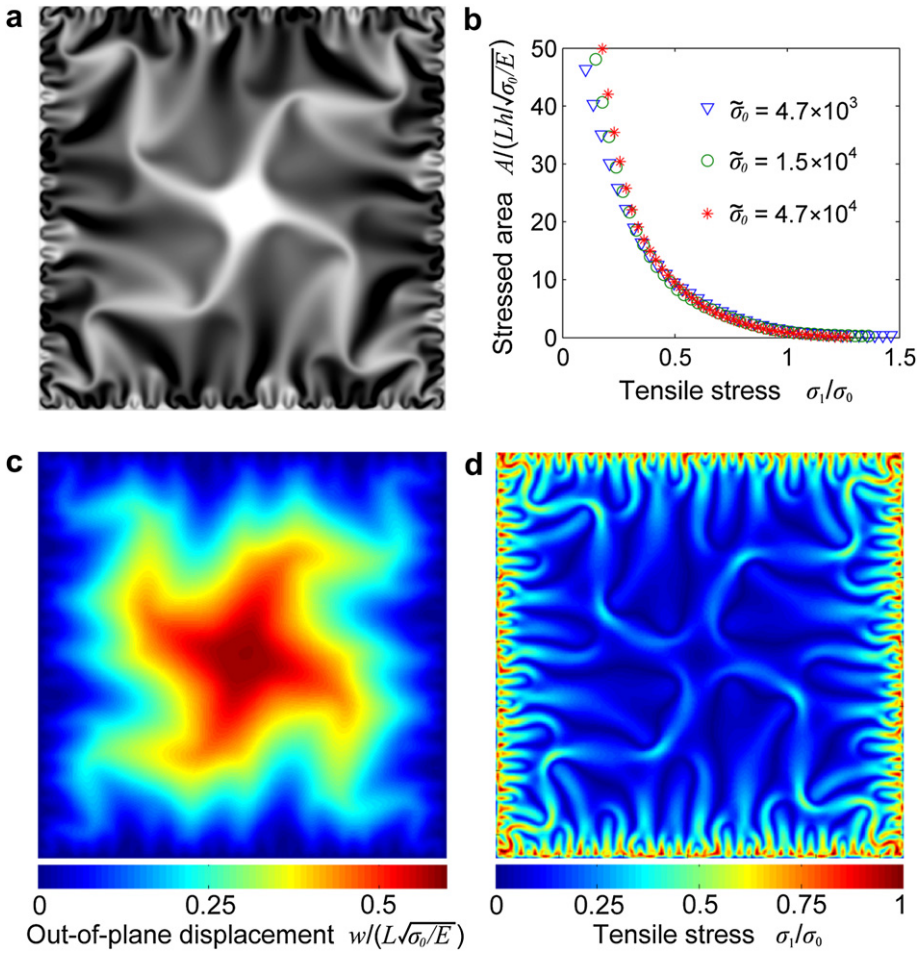

Fig. 4. (a) Modeling configuration of membrane with scaled biaxial stress $\tilde{\sigma}_0 = (\sigma_0/E)(L/h)^2 = 4.7 \times 10^4$. (b) The area in which the tensile stress exceeds σ_1; data is shown for $\tilde{\sigma}_0 = 4.7 \times 10^3$, 1.5×10^4 and 4.7×10^4. The area A is scaled by $Lh/\sqrt{\sigma_0/E}$ and the stress σ_1 is scaled by σ_0. The out-of-plane displacement and distribution of tensile stress for the membrane in (a) are shown in (c) and (d), respectively.

some instances the diagonal reflection symmetry is roughly retained. In our simulations a similar pattern was obtained by incrementing $\tilde{\sigma}_0$ rapidly, thereby allowing less time for full elastic relaxation to occur. The pattern obtained has slightly higher deformation energy than that in Fig. 4(a) and is metastable. Therefore, if this pattern is observed, it is likely that the membrane may further deform to achieve the most energetically stable configuration. We also simulated membranes constrained to reflection symmetry, finding up to 5% higher deformation energy than that of Fig. 4(a). These findings are confirmed by experimentally observed configurations of YSZ, where the pattern shown in Fig. 3(c) is seen after repeated heating cycles and for membranes as thin as 27 nm [4,9]. Heating cycles of thin film YSZ on Si_3N_4 coated Si leads to an additional biaxial film stress due to the thermal expansion mismatch between film and substrate [11,24]. As shown in Fig. 3(d), the magnitude of σ_0 scales directly with film thickness; therefore, for a given deposition rate and edge length, beyond a critical thickness, a stable buckling configuration will emerge, likely similar to that shown in Figs. 3(c) and 4(a). Our findings on the buckling configurations and stability are summarized in Fig. 5.

In the recent work by Evans et al. [10] similar patterns are observed. Their optical micrographs present the metastable cross-like pattern, similar to Fig. 3(b), as well as the stable pattern akin to that in Fig. 3(c). The pattern into which the membrane enters may depend on film deposition methods; we report RF sputtered films, while Evans et al. report films prepared by pulsed laser deposition. This serves well to point out that elastic theories are based on homogeneous materials, therefore the intricacies of real materials that include complex microstructures, grain boundaries, and chemical strain from oxygen non stoichiometry may not be adequately captured and as such, careful, systematic experimental work can be useful. Extremely thin free-standing membranes are also sensitive to external perturbations. For example, pressure difference between the two sides at any point during the

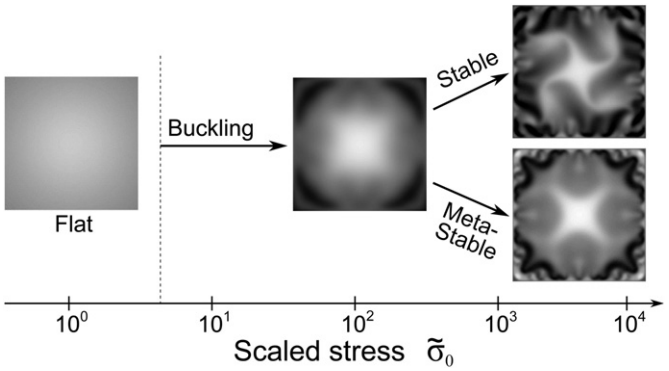

Fig. 5. A flat membrane under biaxial compressive stress buckles first into an axially symmetric configuration. At increasing stress the symmetry either breaks, leading into a stable swastika-like configuration, or persists as a metastable cross-like configuration.

experimental assembly likely affects selection of the pattern. Such pressure transitions in thin, square membranes have been observed previously [25]. With regard to the processing scheme, an important pressure contribution can be traced to the dry etching processing step used to remove the Si_3N_4 support layer.

4.2. Additional considerations for stable membranes

From a practical perspective, a self-supported, thin film membrane operating in the context of electrochemical energy conversion or chemical separation should be under sufficient compression to avoid fracture due to additional stresses imparted from differences in thermal expansion between the film and substrate. This becomes even more complex when multiple dense layers are needed. For example, in TF-SOFCs integrating oxide cathodes, the stress of each layer must be carefully characterized and engineered in order to create stable membrane heterostructures [26]. For the current case, expansion coefficients of both Si and YSZ are temperature dependent, therefore the induced thermomechanical stress will also be a function of temperature and can be expressed by $\sigma_T = \int_{T_1}^{T_2} ((\alpha_{YSZ} - \alpha_{Si})E_f)/(1 - \upsilon_f)dT$, where α_{YSZ}, α_{Si}, and $E_f/1 - \nu_f$ represent the linear expansion coefficient YSZ and Si, and the biaxial modulus of the film, respectively [24]. An estimate of the induced stress at the highest temperature can be obtained using $\sigma_T = (\alpha_{YSZ} - \alpha_{Si})\Delta TE$. For the materials used in our experiments, the linear expansion coefficients at 550 °C of $\alpha_{Si} = 4$ ppm K^{-1}, $\alpha_{YSZ} = 10$ ppm K^{-1} and $\Delta T \approx 525$ K yield $\sigma_T \approx 3.15 * 10^{-3}E$. [27,28]. Ideally, membrane structures going through many thermal cycles for practical application should be designed such that the residual film stress, σ_0, is greater than any thermally generated tensile stress. On the other hand, the inevitable buckling of the membrane under compression leads to bending which may also cause failure. In certain energy applications, failure can be catastrophic; for example, membrane rupture in TF-SOFCs could lead to fuel–air mixing. Rupture in areas with high tensile stress is a significant concern. From Fig. 4(d) it is evident that the highest tensile stresses – determined from the superimposed in-plane and bending stresses – are in the vicinity of the clamped boundaries. The area $L\delta \sim Lh/\sqrt{\sigma_0/E}$ on which the high stress is focused follows from the boundary layer analysis above. We confirm this fact in Fig. 4(b) by collapsing the stress distributions for various σ_0 by scaling the stressed areas by $Lh/\sqrt{\sigma_0/E}$, and find that the extreme tensile stress, i.e. the largest principal stress from coupled in-plane and bending deformations, is comparable to σ_0. Crudely, the ultimate tensile strength of the membrane material should be greater than σ_0 to prevent failure from buckling. However, a detailed reliability study should also take into account randomness in the strength via Weibull analysis. Since the tensile stresses focus on a narrow boundary layer, the membrane shape is expected to have only a weak effect on the mechanical strength. Simulations indicate stressed spots at the corners of our square membrane, shown in Fig. 4(d), however, the peak tensile stress within them is comparable to that elsewhere near the edges. On the other hand, the pattern in the interior of the membrane would depend on the membrane shape.

4.3. TF-SOFCs utilizing ultra-thin membranes

In order to explicitly demonstrate the applicability of such stable, elastically buckled membranes, TF-SOFCs were fabricated with a 100 nm YSZ electrolyte with high surface area, nanoporous Pt layers deposited on both sides of the membrane. The ductility and open structure of these metallic layers is not expected to change the buckling patterns of such membranes or the temperature dependence. This was confirmed and shown in Fig. 6(c) which indicates that the membrane pattern remains similar to the stable configuration after high temperature fuel cell operation. Similar observations of the elastic stability of this buckling pattern on SOFC devices with nanoporous metallic electrodes have been reported for membranes operating for over 50 h at 723 K [29]. To date, there has been no report of natural gas fueled TF-SOFCs to the best of our knowledge. It is an abundant hydrocarbon source and the ability to directly utilize it is promising for near term applications. The oxidant used was standing air, however, using pure O_2 can increase the performance [30]. The *I–V* characteristics of a representative cell are shown in Fig. 6(a). A maximum power density of 108 mW cm^{-2} was achieved at a voltage of 0.37 V operating at 405 °C. The power density was reduced to 47 mW cm^{-2} at 505 °C. As highlighted in previous studies, the onset and subsequent deterioration of performance in TF-SOFCs with pure metallic electrodes is related to the spreading and microstructural re-arrangement of the metal on the oxide surface [9,31,32]. The process of coarsening in a nano-porous metal is complex and can be related to many independent parameters. In the context of TF-SOFCs these include the surface energetics of the oxide–metal interface, type of fuel used, and electro-migration due to high current density. Hence typical studies with metal electrodes allow proof-of-concept demonstration for the utility of these membranes and also may be of interest for applications that require short term operation with high power densities. In this regard, the open circuit voltage (OCV) is an indication of pristine membrane quality and can be expressed by the Nernst equation [30]. For H_2 oxidation, the OCV in this temperature range should be approximately 1 V. Since we have used Pt as the electrocatalyst, fundamentally only gas leakage or electrical shorts through the membrane could play a role in lowering the OCV. Fig. 6(b) indicates that the OCV is nearly perfect across the temperature range tested. Direct comparison to H_2 fuel is also shown and highlights the more rapid decline of the OCV in natural gas fuel, which is discussed further below. The likelihood of microstructural defects, such as pinholes is low since we do not observe voids in any electron micrographs [8,33]. Fig. 6(d) shows a cross-sectional scanning electron image of the dense YSZ layer between porous Pt. Therefore to address small deviations in OCV behavior, the fuel source must be considered. Using a direct hydrocarbon source is more complex than H_2 since the possible mechanisms of oxidation can require multiple steps [34]. Additionally, impurities in the fuel such as sulfur can block active catalytic sites or poison the anode [35]. Deviation from approximately 1 V at higher temperature is likely related to some combination of these secondary factors, which require exit fuel stream analysis. The ability to directly utilize natural gas offers a tangible near term alternative for cleaner energy production, however, fuel utilization should also be considered for efficient usage of the chemical energy source. As described in Section 3, the volumetric flow rate of natural gas was 30 cm^3 min^{-1}. The typical dominant hydrocarbon constituent in natural gas is CH_4 and as such the density of natural gas falls in the 0.7–0.9 kg m^{-3} range [36]. Although the exact redox couple is not known, to make an estimate of the fuel utilization, we assume that CH_4 is only partially internally reformed since the temperature is well below 700 °C and that direct oxidation dominates. At maximum power conditions, the total cell current, which is the sum of nine equivalent membranes on the chip, was approximately 0.7 mA. This corresponds to a fuel utilization of approximately 3%, which is in the range of 1–4% for previously reported fuel utilization of traditional SOFCs operating on natural gas [37]. Although this requires further optimization, the ability to extract power by using the self-supported membrane structure clearly indicates the practical applicability of such structures for future usage.

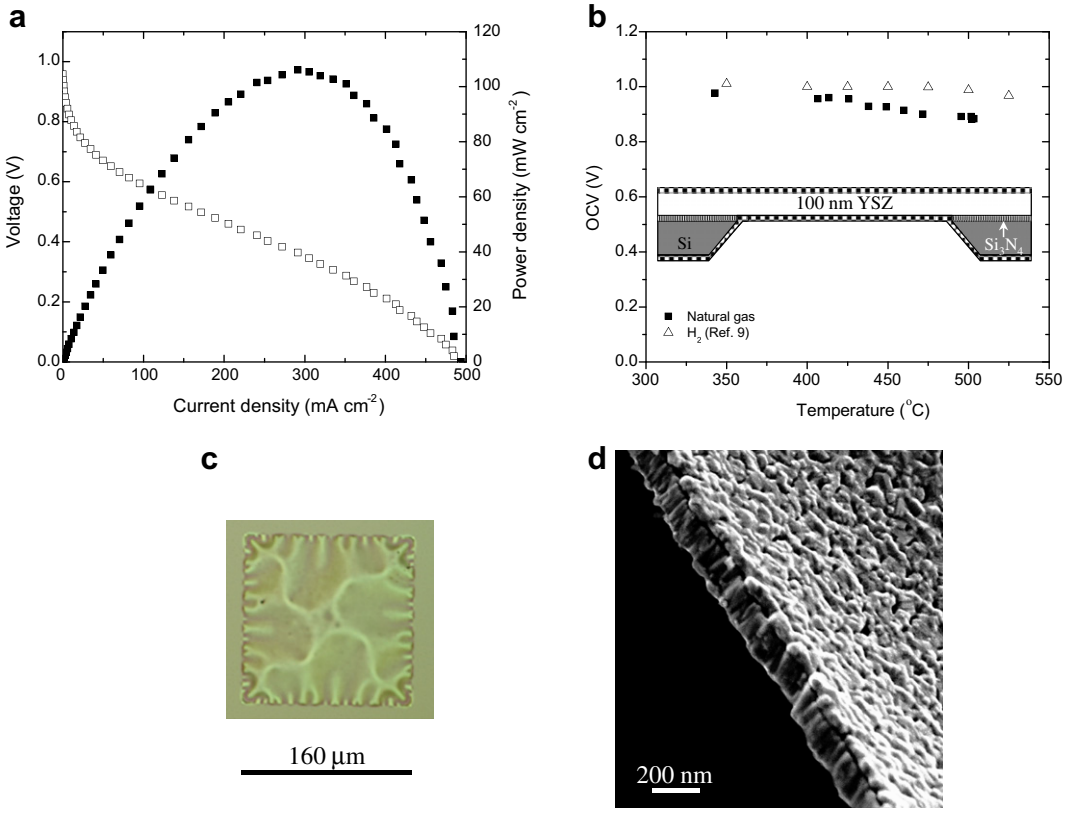

Fig. 6. (a) *I–V* curve of Pt/YSZ/Pt TF-SOFC membrane operating at 405 °C with natural gas as fuel and air as the oxidant. Open and closed symbols represent voltage and power, respectively. (b) The temperature dependence of OCV for the Pt/YSZ/Pt membranes operating in natural gas with reference data for similar cells operating in H_2. The inset shows a cross-sectional schematic of the type of cells being tested. (c) An optical micrograph of the Pt/YSZ/Pt membrane after high temperature TF-SOFC operation, still showing the characteristic 4-fold rotational symmetry. (d) A cross section scanning electron microscope image of the membrane, with dense YSZ sandwiched by porous Pt.

5. Conclusions

Our experimental and theoretical results address stable far-from-onset compression-induced buckling patterns in clamped self-supported membranes. This work elucidates the mechanism by which such patterns are formed, verifies that the deformations are elastic, identifies stress considerations to resist failure, and demonstrates the spatial distribution of highly stressed areas on the membrane. We highlight the buckled configurations acceptable in design of electrochemical devices whose performance depends crucially on the high aspect ratio of their membranes. While decreasing the thickness of the membrane leads to pronounced buckling and focusing of deformations at the boundaries, the highest tensile stresses are comparable to the magnitude of the residual stress σ_0. The pattern with minimal energy has a characteristic rotationally symmetric interior with nearly vanishing stress. Membranes that undergo an applied load, such as repeated thermomechanically induced stress, tend toward a similar configuration, indicating the strong elastic stability of such a pattern. Stable membranes were further used to fabricate thin film solid oxide fuel cells that operate in natural gas. Near ideal thermodynamic potential of these devices indicates the nanoscale membranes are gas-tight and suitable for broad electrochemical applications.

Acknowledgments

We acknowledge NSF Grant CCF-0926148 for financial support. KK was supported by the Department of Defense (DoD) through the National Defense Science & Engineering Graduate Fellowship (NDSEG) Program. The authors are grateful to Professor Robert Wood's lab for confocal microscope usage.

References

[1] S.C. Singhal, K. Kendall, High Temperature Solid Oxide Fuel Cells, Elsevier, Oxford, UK, 2003.
[2] This expression is valid for O^{2-} transport at 500 °C when an overpotential of more than 67 mV is applied and the ionic flux is voltage driven. Below this overpotential, the ionic current can also be concentration driven.
[3] V.T. Srikar, K.T. Turner, T.Y.A. Ie, S.M. Spearing, J. Power Sources 125 (2004) 62–69.
[4] N. Yamamoto, D.J. Quinn, N. Wicks, J.L. Hertz, J. Cui, H.L. Tuller, B.L. Wardle, J. Micromech. Microeng. 20 (2010) 035027.
[5] P.C. Su, F.B. Prinz, Electrochem. Commun. 16 (2012) 77–79.
[6] S. Rey-Mermet, P. Muralt, Solid State Ionics 179 (2008) 1497–1500.
[7] C.W. Kwon, J.I. Lee, K.B. Kim, H.W. Lee, J.H. Lee, J.W. Son, J. Power Sources 210 (2012) 178–183.
[8] A. Evans, A.B. Hutter, J.L.M. Rupp, L.J. Gauckler, J. Power Sources 194 (2009) 119–129.
[9] K. Kerman, B.K. Lai, S. Ramanathan, J. Power Sources 196 (2011) 2608–2614.
[10] A. Evans, M. Prestat, R. Tölke, M.V.F. Schlupp, L.J. Gauckler, Y. Safa, T. Hocker, J. Courbat, D. Briand, N.F. deRooij, D. Courty, Fuel Cells, http://dx.doi.org/10.1002/fuce.201200028.
[11] D.J. Quinn, B. Wardle, S.M. Spearing, J. Mater. Res. 23 (2008) 609–618.
[12] S.P. Timoshenko, Theory of Elastic Stability, Dover, New York, 2009.
[13] L.D. Landau, Theory of Elasticity, Elsevier, China, 1986.
[14] M. Das, A. Vaziri, A. Kudrolli, L. Mahadevan, Phys. Rev. Lett. 98 (2007) 014301.
[15] R.D. Schroll, E. Katifori, B. Davidovitch, Phys. Rev. Lett. 106 (2011) 074301.
[16] T. Tallinen, J. Ojajärvi, J.A. Åström, J. Timonen, Phys. Rev. Lett. 105 (2010) 066102.
[17] E. Cerda, L. Mahadevan, J. Passini, Proc. Natl. Acad. Sci. 101 (2004) 1806–1810.
[18] W. Jin, P. Sternberg, J. Math. Phys. 42 (2001) 192–199.
[19] G.G. Stoney, Proc. Roy. Soc. A 82 (1909) 172–175.
[20] H. Windischmann, J. Appl. Phys. 62 (1987) 1800.
[21] International center for diffraction data, 030-1468.
[22] P.J. Withers, H.K.D.H. Bhadeshia, Mater. Sci. Technol. 17 (2001) 355–365.
[23] V. Ziebart, O. Paul, H. Baltes, J. Microelectromech. Syst. 8 (1999) 423–432.
[24] M. Ohring, The Materials Science of Thin Films, Academic, New York, 1991.
[25] T. Kramer, O. Paul, J. Micromech. Microeng. 12 (2002) 475–478.
[26] B.-K. Lai, K. Kerman, S. Ramanathan, J. Power Sources 195 (2010) 5185–5196.
[27] H. Hayashi, T. Saitou, N. Maruyama, H. Inaba, K. Kawamura, M. Mori, Solid State Ionics 176 (2005) 613–619.

[28] Y. Okada, Y. Tokumaru, J. Appl. Phys. 56 (1984) 314.
[29] K. Kerman, B.K. Lai, S. Ramanathan, J. Power Sources 202 (2012) 120–125.
[30] J. Newman, K.E. Thomas-Alyea, Electrochemical Systems, Wiley, New York, 2004.
[31] X. Wang, H. Huang, T. Holme, X. Tian, F.B. Prinz, J. Power Sources 175 (2008) 75–81.
[32] Y. Takagi, B.K. Lai, K. Kerman, S. Ramanathan, Energy Environ. Sci. 4 (2011) 3473–3478.
[33] I. Garbayo, G. Dezanneau, C. Bogicevic, J. Santiso, I. Gracia, N. Sabate, A. Tarancon, Solid State Ionics 216 (2012) 64–68.
[34] O.A. Marina, M. Mogensen, Appl. Catal. A: Gen. 189 (1999) 117–126.
[35] K. Haga, S. Adachi, Y. Shiratori, K. Itoh, K. Sasaki, Solid State Ionics 179 (2008) 1427–1431.
[36] R.E. Sonntag, C. Borgnakke, G.J. Van Wylen, Fundamentals of Thermodynamics, Wiley, New York, 2002.
[37] J. Liu, S.A. Barnett, Solid State Ionics 158 (2003) 11–16.